Simulating high-entropy alloys at finite temperatures: An uncertainty-based approach

Andrew Novick,[1] Quan Nguyen,[2] Roman Garnett,[2] Eric Toberer,[1] and Vladan Stevanović[3,*]
[1]*Department of Physics, Colorado School of Mines, Golden, Colorado 80401, USA*
[2]*Department of Computer Science and Engineering, Washington University in St. Louis, St. Louis, Missouri 63130, USA*
[3]*Department of Metallurgical and Materials Engineering, Colorado School of Mines, Golden, Colorado 80401, USA*

(Received 1 December 2022; accepted 5 May 2023; published 5 June 2023)

A general method is presented for modeling high-entropy alloys as ensembles of randomly sampled, ordered configurations on a given lattice. Statistical mechanics is applied *post hoc* to derive the ensemble properties as a function of composition and temperature, including the free energy of mixing and local structure. Random sampling is employed to address the high computational costs needed to model alloys with a large number of components. Doing so also provides rigorous convergence criteria, including the quantification of noise due to random sampling, and an estimation of the number of additional samples required to lower this noise to the desired levels. Binary to five-component alloys of the group-IV chalcogenides are used as case examples, for which the predicted miscibility shows excellent agreement with experiment. This method is well-suited for calculating the configurational thermodynamics, local structure, and ensemble properties of complex alloys, and it is attractive for materials with temperature-dependent, short-range order.

DOI: 10.1103/PhysRevMaterials.7.063801

I. INTRODUCTION

From a materials design perspective, alloying provides a continuous composition space over which multiple conflicting properties can be simultaneously optimized. This flexibility has allowed for semiconducting alloys to have a wide variety of applications, including use in LEDs, solar cells, batteries, and thermoelectric generators [1–4]. Increasingly, this desire for multiproperty optimization encourages the exploration of high-entropy alloys [5]. The complexity of these chemical spaces necessitates computational guidance with respect to alloy stability, local and long-range structure, and material properties. For alloys with fewer components, *ab initio* methods such as special quasirandom structures, cluster expansion, and the independent cell approximation are effective in guiding experimental efforts [6–9]. Each of these approaches faces significant challenges when moving to higher dimensions; this work presents how the independent cell approximation can be modified to efficiently explore high-dimensional alloys.

The special quasirandom structure (SQS) approach uses a single supercell whose atomic arrangement is optimized to emulate a fully disordered (random) alloy structure within the constraints of periodic boundary conditions [6]. Alloying on both sublattices of an ionic system can result in short-range order due to the diversity of constituent atom sizes and interactions; as such, the complete disorder approximation of SQS overestimates the enthalpy of mixing [1,10]. Further, no information on entropy is provided–the analytic approach associated with SQS overestimates entropy by assuming a fully random alloy [5], disregarding any possibility for correlated disorder or short-range order [11,12].

Despite these stability challenges, the use of a single supercell allows for the full suite of plane-wave based DFT methods to predict material properties. However, the extremely large supercells required for complex alloys quickly become computationally costly since DFT scales with the number of atoms as $O(N^3)$.

Unlike SQS, cluster expansion (CE) does not assume complete disorder; instead, a model Hamiltonian is fit with a series of total-energy calculations on a number of small supercells of varying configurations and compositions. An accurate model Hamiltonian is a powerful tool—with it, the calculation of arbitrarily large supercells of varying configurations becomes almost effortless. Coupled with Monte Carlo, a model Hamiltonian can be used to predict the order-disorder behavior across the modeled alloy composition space, all as a function of synthesis-temperature [13–17]. This is particularly useful for studying systems with short-range order. Still, the number of interaction parameters required to fit a cluster expansion grows with the number of alloyed elements, necessitating more calculations. The large number of calculations makes the method costly—and even prohibitive—for high-entropy spaces. Furthermore, the model Hamiltonian does not provide predictions on the overall structure of the alloy. In the field of semiconducting alloys, the extended strain fields and distortions arising from alloying are important for the ways in which they affect transport properties and band dispersions [18–21].

Within the independent cell approximation (ICA), the material is modeled as an ensemble of ordered configurational states, as illustrated in Fig. 1 [8,9,22]. Specifically, calculations are first run on multiple supercells of varying configurations at or near a single composition. The probability of each configurational state is then calculated using statistical mechanics. Finally, the material properties are calculated by taking the weighted average over the configurations. In contrast to CE, no model Hamiltonian is

*vstevano@mines.edu

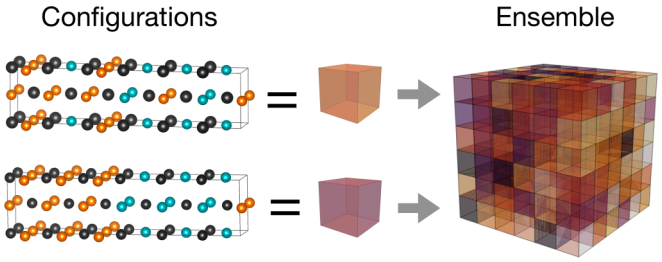

FIG. 1. Alloys are represented as an ensemble of configurational states within the independent cell approximation. *Post hoc* application of statistical mechanics then predicts the alloy's local structure, thermodynamic stability, and material properties.

fit; the ensemble properties are derived directly from the cells within the ensemble. By avoiding the rigid lattice assumed by CE, the resulting ensemble averages can describe local structural distortions arising from disorder (e.g., deviations in bond lengths, bond angles, and local volumes). The ICA has been successfully used in a variety of applications: alloying [8,22–25], composition disorder [9], spin disorder [26,27], metastable polymorphs [28–30], and glasses [31,32]. Furthermore, a broad range of ensemble properties have been calculated using the ICA. These include structure-based properties like x-ray diffraction patterns and radial distribution functions [31], mechanical properties [24], magnetic structure [27], thermomechanical properties [33], and phonons [34].

In the context of alloys, there has been considerable diversity in how ICA is implemented. Key differences have involved supercell size, sampling of the configurational space, and the treatment of configurational entropy. An early example of ICA by Jiang *et al.* sought to replicate large SQS of inverse spinels with relatively few smaller supercells; the contributions of these supercells were weighed such that the correlation function of the ensemble resembled a fully random alloy [8]. Using just two 28-atom supercells was sufficient to determine an ensemble energy that agreed with both a 168-atom SQS and a cluster expansion (with a cross-validation error of 3.4 meV/formula unit). By focusing on matching a large SQS cell, this embodiment of ICA is not able to interrogate the temperature dependence of local structure and properties.

In addition to reproducing SQS results, ICA also has the capability of measuring configurational entropy. Leder *et al.* fit various ICA configurations to a cluster expansion in order to estimate the solubility as a function of temperature [23]; however, cluster expansion in high-entropy spaces is computationally expensive. Sarker *et al.* developed an approximation for the configurational entropy that directly uses ICA results, termed the "entropy forming ability" (EFA). This metric is based on the spread of the supercell energies. In this work, the metric is applied to 56 high-entropy carbides ($V_{0.2}W_{0.2}X_{0.2}Y_{0.2}Z_{0.2}C$); experimental formation of homogeneous alloys was found to correlate with EFA magnitude, regardless of the enthalpy of mixing. As these carbides all have the same configurational entropy in the high-temperature limit, this work highlights the importance of considering the configurational entropy at finite temperatures.

This paper addresses opportunities for improving the ICA, with a focus on (i) quantitatively determining configurational entropy, and thus the free-energy convex hull; (ii) accurately modeling local structural distortions; and (iii) exploring high-dimensional chemical spaces. In all cases, this is made computationally tractable by randomly sampling a portion of the configurational space, thus allowing for the use of larger, more disordered supercells within a first-principles framework.

First, $PbSe_{0.5}Te_{0.5}$ and $PbS_{0.5}Te_{0.5}$ are used as a way of illustrating the methodology. These compositions are chosen because they have sufficiently few configurations. Therefore, ensemble statistics can be derived from completely sampling all possible configurations for a given supercell size. Convergence tests are then run to determine the necessary supercell size and number of configurations needed to capture the configurational thermodynamics and local structure of these IV-VI alloys. With complete sampling as a benchmark, random sampling is then conducted on the same systems with far less computational cost and little added uncertainty. The uncertainty due to random sampling is then derived by using the central limit theorem [35,36] in order to quantify the robustness of the result. With a rational approach to random sampling in hand, this example is extended to the pseudoternary, $PbS_xSe_yTe_{1-x-y}$. The temperature-dependent phase diagram is calculated and matches well with experiment. Finally, the computational tractability of this method in high-entropy spaces is illustrated through the exploration of the quintary, $(Pb_{1-x}Ge_x)(Te_ySe_zS_{1-y-z})$.

II. METHODS

An overview of the presented method is shown in Fig. 2. First, the initial conditions are established. Alloy configurations are then randomly sampled from the set of total configurations. Total-energy calculations are run on the configurations, plus the additional calculations that are needed to compute the properties of interest. Then, the temperature-dependent probabilities of these configurations are determined using statistical mechanics. The ensemble properties are derived from the probabilities of the configurations and their properties. For the property of interest, the uncertainty in the prediction is estimated using the central limit theorem. If the uncertainty is above the specified convergence criteria, the central limit theorem is used to determine the number of additional configurations that are needed. Finally, these calculations are conducted, and the ensemble property is reevaluated.

A. Configuration sampling

As referenced in the first panel of Fig. 2, the desired composition, structure-type, supercell size, and number of initial configurations are specified. The convergence property and criteria need to be specified as well, but we will discuss this in Sec. II C. For a given supercell size, a number of symmetry-inequivalent supercells are constructed. This is done by using the algorithm developed by Hart and Forcade [37], which produces hermite normal form transformation matrices that correspond to symmetry-inequivalent supercells. A complete list of possible decorations is then built for each supercell. Here, a configuration is defined as the pairing of a supercell and a decoration. The size of the complete set of configurations is simply the product of the number of supercells and

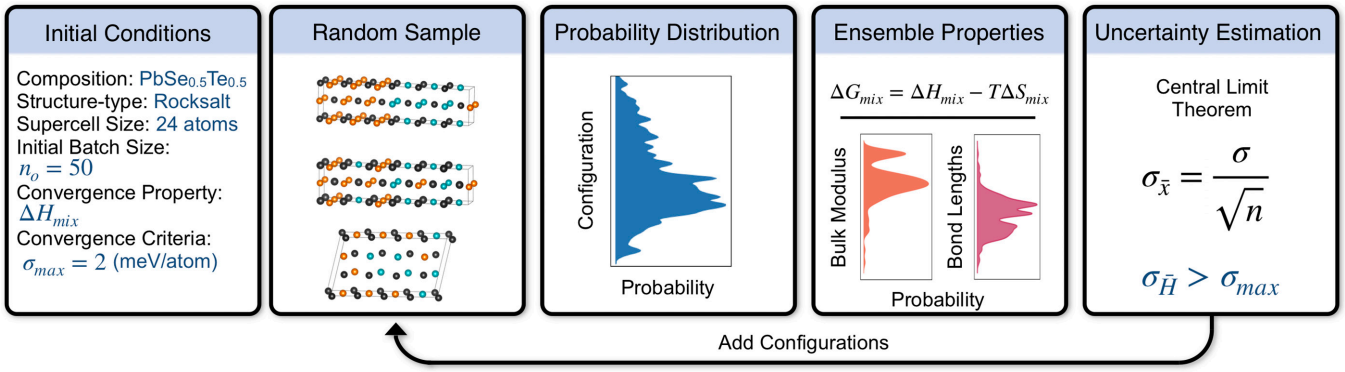

FIG. 2. The methodology developed herein begins with specifying the initial conditions; random configurations are then generated within those constraints. The $\Delta H_{\mathrm{mix},i}$ and the temperature-dependent probability of each configuration are calculated. The properties of interest are then determined using ensemble averaging. Additionally, ΔG_{mix} is calculated to determine stability with respect to the free-energy convex hull. The central limit theorem is then applied to estimate the uncertainty in the predictions ($\sigma_{\bar{X}}$) and the number of new configurations that may be needed to further reduce the uncertainty below the convergence criteria, σ_{max}.

decorations. A randomly chosen configuration is one that is sampled from this set.

All transformation matrices used provide symmetry-inequivalent supercells, but once decorations are applied, some configurations will be symmetrically equivalent. Both translational and rotationally symmetric configurations are included in the ensemble. They are interpreted to be degenerate, and thus should be counted within the ensemble, as is done elsewhere [22]. Finally, the chosen configurations are subjected to full structural relaxations, which was done using VASP [38]. The generation of configurations was executed in Python using the PYLADA software [39]. The numerical approaches used in this work are described in detail in Sec. II D.

B. Probability distribution and ensemble properties

The first step is to calculate the partition function, Z:

$$Z = \sum_{i}^{n} e^{-E_i/k_B T}, \tag{1}$$

where i is the configuration index, n is the total number of configurations sampled, E_i is the total energy per formula unit of a given configuration, k_B is Boltzmann's constant, and T is the absolute temperature. The ensemble probability of the ith configuration, P_i, is

$$P_i = \frac{e^{-E_i/k_B T}}{Z}. \tag{2}$$

Illustrated in Fig. 3 are the ensemble probabilities of 50 configurations of $PbSe_{0.5}Te_{0.5}$. The probability of the ground-state configuration approaches unity as temperature decreases, while in the high-temperature limit, the probability of each configuration asymptotes to n^{-1}. Generally, the ensemble average of a property, $\tilde{X}_n$, is given by taking the weighted average over n configurations,

$$X = \sum_{i}^{n} P_i X_i. \tag{3}$$

Depending on the property, ensemble averaging may require more nuanced averaging—for example, the ensemble radial distribution function in [31].

Importantly, when the entropy or free energy of mixing are mentioned, they refer to the configurational free energy and entropy. Vibrational degrees of freedom are not considered here. As Esters *et al.* show, vibrational entropy should be considered when the parent compounds have different nearest-neighbor environments from the resulting alloy [34]. This is not the case in our work, since we consider rocksalt alloys and parent compounds that are either rocksalt or distorted versions of rocksalt. The exclusion of the vibrational degrees of freedom may affect the accuracy of the mixing temperatures.

The configurational free energy of mixing, ΔG_{mix}, can be calculated from the partition function in a standard way:

$$\Delta G_{\mathrm{mix}} = -k_B T \ln(Z) - \sum_{j}^{K} E_j x_j. \tag{4}$$

This value will need to be adjusted once the ΔS_{mix} correction is applied. In this work, we will be referring to pure

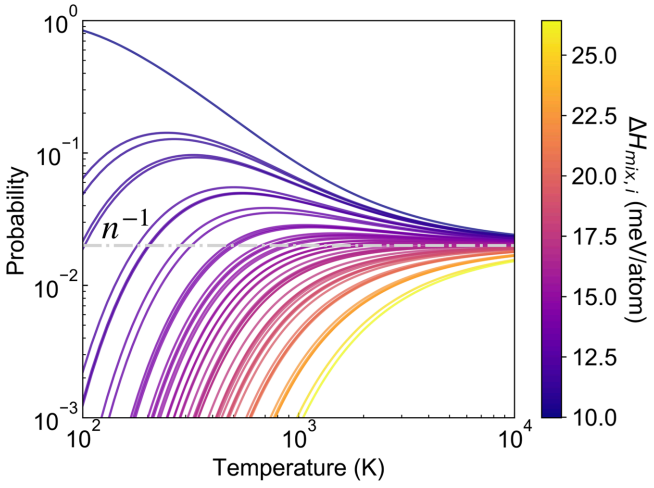

FIG. 3. Within a given ensemble, the variation in $\Delta H_{\mathrm{mix},i}$ leads to significant temperature evolution of the probability for each configuration. In the high-temperature limit, the probabilities converge to n^{-1}. Here, an ensemble of 50 $PbSe_{0.5}Te_{0.5}$ configurations is considered, with each configuration represented by a line colored by its $\Delta H_{\mathrm{mix},i}$.

constituents that make up the alloy as parent compounds, but the framework presented here would also apply if only elements were being alloyed. Here, j counts over parent compounds of the alloy, x_j is the fraction of the alloy made up by that parent, and E_j is the total energy of the parent. Finally, K is the number of parents that comprise the alloy. The enthalpy of mixing, $\Delta H_{\mathrm{mix},i}$, for configuration i is defined in the following equation:

$$\Delta H_{\mathrm{mix},i} = (E_i + pV_i) - \sum_j^K x_j(E_j + pV_j). \tag{5}$$

Here, p is the pressure and V_i and V_j are the volumes per formula unit. All results presented here correspond to the low-pressure ($p \approx 0$) case for which internal energy and enthalpy are equal, as are the Helmholtz and Gibbs free energies. The formalism can easily be extended to elevated pressures by computing the equations of state, $E(V)$, for both the randomly sampled configuration and their parent compounds.

ΔH_{mix} for the ensemble is then defined by ensemble averaging over all $\Delta H_{\mathrm{mix},i}$. Next, the entropy of mixing, S_{mix}, can be calculated from the ensemble-averaged enthalpy of mixing ΔH_{mix} and the free energy of mixing:

$$\Delta S_{\mathrm{mix}}(T) = \frac{\Delta H_{\mathrm{mix}}(T) - \Delta G_{\mathrm{mix}}(T)}{T}. \tag{6}$$

ΔS_{mix}, ΔG_{mix}, and to a lesser extent ΔH_{mix} are dependent on the number of configurations sampled. Random sampling approximates well the distribution of energies, and hence, its ensemble average. Thus, ΔH_{mix} will remain relatively constant after convergence with respect to the number of configurations has been achieved. However, ΔS_{mix}, and consequently ΔG_{mix}, will change because the partition function increases monotonically with the number of configurations.

To remove the dependency of ΔS_{mix} on the number of randomly sampled configurations, a scaling factor is applied to ΔS_{mix} so that it always asymptotes to the configurational entropy in the high-temperature limit, which is analytically known. This value, which we will call ΔS_∞, can be calculated using the standard formula for the configurational entropy of fully random alloys:

$$\Delta S_\infty = -k_B \sum_i x_i \ln(x_i), \tag{7}$$

where i is a parent compound of the alloy and x_i is its alloy fraction. A scaling factor, d, is defined as

$$\frac{\Delta S_\infty}{\Delta S_{\mathrm{mix}}(T \to \infty)} = d. \tag{8}$$

In this work, $T = 2000$ K is sufficiently high such that the entropy has asymptoted. This temperature was chosen based on the inspection of the systems present in this paper, but it may need to be reconsidered for other systems. The scaling factor is then applied to the entire ΔS_{mix} curve. From there, the free energy of mixing can then be recalculated using this scaled final entropy of mixing.

C. Central limit theorem and supercell size

When faced with an overwhelmingly large configurational space, random sampling is one approach to render the number of calculations tractable. Random sampling can be viewed as an acceptable approximation under the following condition. For a property of interest, X, the ensemble average derived from n randomly sampled configurations, X_n, is in agreement with the ensemble average of the total distribution of configurations, X_{tot} (i.e., $X_n \approx X_{\mathrm{tot}}$). In practice, however, X_{tot} will not be available. Therefore, an alternative method for verifying random sampling is required.

The central limit theorem (CLT) offers one such path [35,36]. The CLT states that if the above random sampling procedure were repeated infinitely many times, the resulting distribution of X_n values would have three main characteristics. It would be (i) approximately a Gaussian distribution that is (ii) centered around the true mean, X_{tot}, and (iii) the distribution would have a standard deviation of $\sigma_{X,n}$. Critically, $\sigma_{X,n}$ is the uncertainty in our X_n prediction due to random sampling. Evaluating $\sigma_{X,n}$ will be crucial for justifying the random sampling implemented in this work.

The CLT allows us to do this; in the limit as $n \to \infty$, the CLT states

$$\sigma_{\bar{X},n} = \frac{\sigma_{X,\mathrm{tot}}}{\sqrt{n}}. \tag{9}$$

For finite n, Eq. (9) is an approximation. However, the left side of Eq. (9) asymptotes to the right side for fairly small n. Often, an n of 30 is deemed sufficient such that Eq. (9) holds [40,41]. As will be shown in Fig. 4, our numerical simulations for the systems in this work are in general agreement; we illustrate that using $n \geqslant 20$ results in $\bar{X}$ distributions that are approximately Gaussian with standard deviations that agree with Eq. (9).

We will now be moving on to the second approximation within the CLT. Given a particular ensemble of n randomly chosen configurations, where property X has been calculated for each configuration, the resulting distribution of X values has a standard deviation of $\sigma_{X,n}$. When n is sufficiently large, the following approximation can be made:

$$\sigma_{X,n} \approx \sigma_{X,\mathrm{tot}}. \tag{10}$$

$\sigma_{X,n}$ is approximately equal to $\sigma_{X,\mathrm{tot}}$, as will be shown in Sec. III. In this way, the uncertainty of $\bar{X}$ can be estimated from one sufficiently large ensemble of configurations.

In practice, a modestly large ensemble of initial size n_o is built and the above approximation is made. If the uncertainty in $\bar{X}$ is larger than desired, one can rearrange Eq. (9) using the desired $\sigma_{\bar{X},n}$ and σ_{X,n_o} to estimate the additional calculations needed to achieve the desired uncertainty. After the additional calculations are completed, one can reassess the uncertainty using Eq. (9). Overall, the described approach efficiently establishes $\bar{X}$ within the desired uncertainty, while keeping the number of calculations to a minimum.

In applying the CLT to the independent cell approximation, we will need to determine an appropriate n_o that is sufficiently large to estimate $\sigma_{X,\mathrm{tot}}$ while remaining computationally efficient. In practice, one needs to perform a proper convergence test to find a suitable n_o. In our work, we determine the appropriate n_o in a different way by using an exhaustive enumeration of all configurations, which is done to illustrate the methodology and compare our findings with exact results.

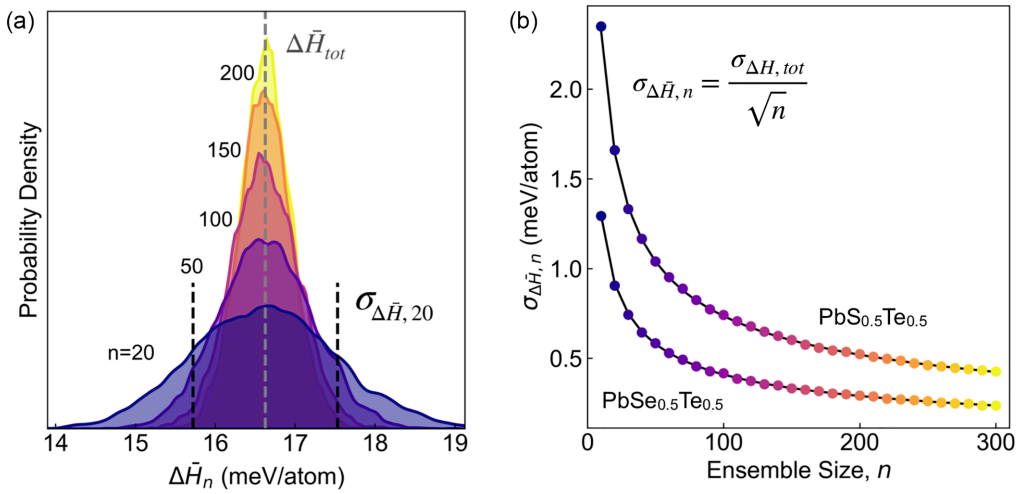

FIG. 4. To illustrate the CLT, we start with the composition $PbSe_{0.5}Te_{0.5}$ and highlight in (a) that the distribution of $\Delta\bar{H}_n$ values for any given n forms a Gaussian centered around the true value, $\Delta\bar{H}_{\text{tot}}$. The standard deviation of each Gaussian, $\sigma_{\Delta\bar{H},n}$, decreases with increasing n. Each Gaussian arises from calculating $\Delta\bar{H}_n$ of 10 000 ensembles. Each point in (b) is determined by taking the standard deviation in $\Delta\bar{H}$ from 10 000 ensembles, including the Gaussians in (a). In (b), this decrease in $\sigma_{\Delta\bar{H},n}$ can be modeled using the central limit theorem (black line). By simply knowing the ensemble size and $\sigma_{\Delta H,\text{tot}}$, $\sigma_{\Delta\bar{H},n}$ can be determined. The procedure is repeated for $PbS_{0.5}Te_{0.5}$ to illustrate the importance of chemical composition. Since $\sigma_{H,\text{tot}}$ is larger, $PbS_{0.5}Te_{0.5}$ requires more configurations to reach the same level of uncertainty.

A significant portion of Sec. III will be centered around the thermodynamics of mixing. We therefore chose to illustrate CLT with ΔH_{mix}. Here we use the high-temperature limit of ΔH_{mix} [$\Delta H_{\text{mix}}(T \to \infty) = \Delta\bar{H}$], such that $\Delta\bar{H}$ is the simple average of $\Delta H_{\text{mix},i}$ across all sampled configurations. We use the $\Delta H_{\text{mix},i}$ of all ∼37 000 24-atom configurations of $PbSe_{0.5}Te_{0.5}$ to make our total distribution. From the total distribution, 10 000 different ensembles of n configurations are randomly generated and the corresponding 10 000 $\Delta\bar{H}_n$ values are calculated. Furthermore, as shown in Eq. (9), the standard deviation in the distribution of the 10 000 $\Delta\bar{H}_n$, $\sigma_{\Delta\bar{H},n}$, changes as a function of n. To illustrate this effect, we performed the above procedure, building 10 000 ensembles for various n, ranging from 20 to 300. Although we use the high-temperature limit for simplicity of illustration, the CLT can be applied for any temperature; the standard deviation must reflect that not all configurations have equal probabilities. As spoken about in Sec. IV, doing so requires further caution around sampling.

Figure 4(a) shows the associated distributions of $\Delta\bar{H}_n$ values for various n. All of the distributions form an approximate Gaussian, as expected from the CLT. If the number of ensembles were infinite instead of 10 000, the distributions would truly be Gaussians. As n increases from 20 samples per ensemble to 300, it is apparent that $\sigma_{\Delta\bar{H},n}$ decreases. In other words, if one were to randomly sample 20 configurations of $PbSe_{0.5}Te_{0.5}$, there is a large range of probable $\Delta\bar{H}_{20}$ values that could occur, while sampling 200 configurations would significantly narrow this range.

Figure 4(b) further illustrates how the size of n reduces uncertainty in the calculation of $\Delta\bar{H}_n$. The standard deviation of each Gaussian, $\sigma_{\Delta\bar{H},n}$, in panel a is plotted, as well as for many other n that were not shown in panel a. For comparison, the same procedure was repeated for $PbS_{0.5}Te_{0.5}$, which has a larger $\sigma_{\Delta H,\text{tot}}$. The two lines plotted in Fig. 4(b) are generated from Eq. (9).

Composition affects uncertainty as well. The uncertainty in $\Delta\bar{H}$ is smaller for $PbSe_{0.5}Te_{0.5}$ than $PbS_{0.5}Te_{0.5}$, reflecting the wider distribution of configurations in the latter. For a given uncertainty criteria, $PbS_{0.5}Te_{0.5}$ requires more samples. However, for $\Delta\bar{H}$ in the studied systems, the uncertainty is kept below 3 meV/f.u. across the entire composition space using just 50–55 configurations. We employ the CLT throughout the work. In Fig. 6, we will return to the CLT and illustrate that $\sigma_n \approx \sigma_{\text{tot}}$ is a reasonable approximation to make within the context of our method.

Supercell size. Using a sufficiently large supercell size is crucial for calculating the ensemble properties of an alloy. The ensemble statistics can widely vary depending on the supercell size chosen, as will be shown in Fig. 7. The following procedure was adopted for determining the appropriate supercell size. First, evaluate the properties of interest using an SQS for the specified structure type and composition. It is important to make sure the SQS is properly sized as well. Second, for the same composition and structure type, run a series of randomly sampled configurations. Using the CLT, iteratively add samples until the high-temperature ensemble-average result is sufficiently converged. This high-temperature ensemble average should match up well with SQS. If it does not, then repeat the same procedure with configurations of a larger supercell size until the high-temperature ensemble average and the SQS values are within the needed uncertainty.

D. Computational details

Structural relaxations and total energy calculations are conducted within VASP [38], using the PBE functional [42] within the projector-augmented wave method [43]. All structural degrees of freedom were allowed to be optimized within the structural relaxation (i.e., volume, cell shape, atom positions). A plane-wave cutoff of 340 eV and a γ-centered k-point

mesh are used such that the energy is converged to within 3 meV/atom.

We use the AFLOW-POCC method [22] for conducting complete sampling for $PbSe_{0.5}Te_{0.5}$ and $PbS_{0.5}Te_{0.5}$. The SQS structure was generated using Monte Carlo SQS (MCSQS) within the ATAT framework [44]. Clusters were randomized up to the sixth nearest neighbors for pairwise interactions, and first nearest neighbors for threewise interactions. The bulk modulus was calculated by fitting the Birch-Murnaghan equation of state. For a given structure, this involved generating multiple volumes near the minimum volume of the structure and calculating the energy of those volumetrically scaled structures. The equation of state was then fit from those total energy calculations [45,46]. The ensemble bulk modulus was calculated by taking the Reuss average over all configurations. The Reuss average was used since it assumes that all configurations are under equivalent stress [47]. For $PbSe_{0.5}Te_{0.5}$, the bulk modulus was calculated for all configurations with supercell sizes up to 20 atoms. For 24-atom supercells, the bulk modulus was calculated for 200 randomly sampled configurations instead of all 1107 nondegenerate configurations in order to keep the test computationally affordable.

Determining the coordination number of an atom inherently requires making a somewhat arbitrary decision about what atoms are considered to be nearest neighbors. Our method is the following: for a given atom, we find the closest neighboring atom, set that as our base bond length, and only include other atoms into the first shell of coordination if their distance from the central atom is within 20% of the base bond length. We find that a tolerance of 20% helps to capture distorted bonding environments while excluding the second coordination shell.

III. RESULTS

We will be working through multiple case examples to validate this method and illustrate its various applications. To start, we will study a single composition, $PbSe_{0.5}Te_{0.5}$, before moving on to the complete $PbSe_{1-x}Te_x$ pseudobinary where we will derive the free energy of mixing across the composition space, all as a function of temperature. Subsequently, the Pb-chalcogenide pseudoternary ($PbS_{1-x-y}Se_xTe_y$) will be explored to show broader trends and the use of the free-energy convex hull as it compares to experiment. Finally, a high-entropy system, $(Pb_{1-x}Ge_x)(Te_ySe_zS_{1-y-z})$, will be studied.

A. $PbSe_{0.5}Te_{0.5}$

For the single composition $PbSe_{0.5}Te_{0.5}$, we will be focusing primarily on the thermodynamics of mixing. To show that the results are sufficiently converged with respect to random sampling, the CLT will be used. We take this opportunity to illustrate the main assumptions of the CLT within the context of this method. Next, the supercell size necessary to capture accurately the thermodynamics of mixing needs to be determined; we thus calculate the high-temperature ensemble averages for varying supercell sizes and compare them to the SQS value. Finally, we briefly illustrate the dependence of ensemble supercell size on the bulk modulus. This is done to illustrate the importance of moving to larger supercells when considering ensemble properties beyond thermodynamics.

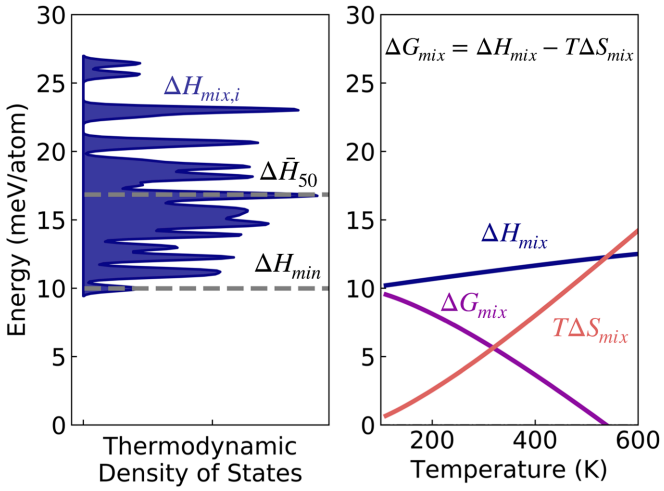

FIG. 5. The distribution of $\Delta H_{\mathrm{mix},i}$ is shown in the left panel, made from an ensemble of 50 $PbSe_{0.5}Te_{0.5}$ configurations. $\Delta \bar{H}_{50}$ denotes the average $\Delta H_{\mathrm{mix},i}$, and ΔH_{min} shows the ground-state configuration. In the right panel, the ensemble ΔH_{mix} gradually moves towards $\Delta \bar{H}_{50}$ as the temperature increases. The entropic contributions ($T\Delta S_{\mathrm{mix}}$) and the resulting free energy ΔG_{mix} are also shown. For temperatures at which ΔG_{mix} is below zero, the alloy is stable against decomposition to its parent compounds (i.e., PbSe and PbTe).

1. *Thermodynamics of mixing*

The thermodynamics of mixing for $PbSe_{0.5}Te_{0.5}$ was calculated according to the equations in Sec. II B. In Fig. 5, the thermodynamic density of states (TDOS) in the left panel shows the distribution of states resulting from 50 randomly sampled configurations. The resulting ensemble ΔH_{mix}, ΔS_{mix}, and ΔG_{mix} are shown in the right panel. At 0 K, ΔH_{mix} is equal to the ground-state configuration at that composition. As the synthesis temperature increases, ΔH_{mix} rises towards the high-temperature limit ($\Delta H_{\mathrm{mix}} = \Delta \bar{H}_{50}$). The ΔS_{mix} rises across this temperature range as the sampling of higher-energy configurations increases. At 600 K, the entropy is 80% of the high-temperature limit and reaches 90% by 1000 K. The ΔG_{mix} becomes negative at ~540 K, and thus will not decompose into its parent compounds after that temperature. However, a negative ΔG_{mix} does not necessarily imply that the composition will be stable. Later sections will show the importance of using the free-energy convex hull in determining stability.

2. *Determining sufficient n_o for CLT*

As stated in Sec. II, a convergence test must be conducted in order to show that the number of randomly sampled configurations in the initial ensemble, n_o, is sufficiently large to satisfy Eq. (10). Here, we run a more advanced convergence test by assembling statistics on $\sigma_{\Delta H,n}$ values on 10 000 unique ensembles of $PbSe_{0.5}Te_{0.5}$ and $PbS_{0.5}Te_{0.5}$.

Figure 6 assesses how $\bar{\sigma}_{\Delta H,n}$ changes with increasing ensemble size and compares this result to $\sigma_{\Delta H,\mathrm{tot}}$, derived from all configurations within the complete distribution. As n

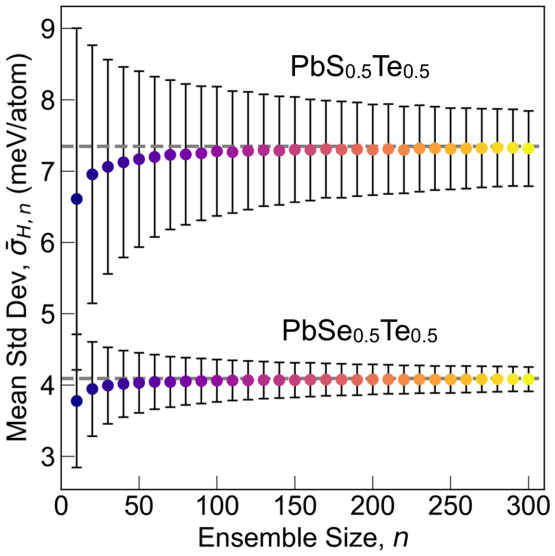

FIG. 6. Given the complete ensemble, there is a standard deviation in the values of ΔH_{mix} ($\sigma_{H,\text{tot}}$) denoted by the horizontal gray dashed lines. With increasing ensemble size, the mean standard deviation $\bar{\sigma}_{H,n}$ rapidly approaches $\sigma_{H,\text{tot}}$. However, the $\sigma_{H,n}$ of a single ensemble shows greater variation as denoted by the error bars, corresponding to $\pm$ one standard deviation from the mean. The small variation from $\sigma_{H,\text{tot}}$ highlights the accuracy of the approximation of Eq. (10). The larger variation in $\sigma_{H,n}$ for $PbS_{0.5}Te_{0.5}$ arises from a broader distribution of ΔH_{mix} values in the complete ensemble.

increases, $\bar{\sigma}_{\Delta H,n}$ quickly asymptotes to $\sigma_{\Delta H,\text{tot}}$. The error bars represent one standard deviation from $\bar{\sigma}_{\Delta H,n}$. Further, the error bars shrink, corresponding to a decrease in the uncertainty of $\sigma_{\Delta H,n}$ for a given ensemble. For n of 50 configurations and above, the uncertainty in the estimates of $\sigma_{\Delta H,\text{tot}}$ is fairly small. As the uncertainty decays, we can increasingly justify the assumption of Eq. (10). To actually assess the uncertainty contribution from making the approximation in Eq. (10), the error bars in Fig. 6 can be divided by $\sqrt{n}$. For instance, consider an $n = 50$ ensemble of $PbS_{0.5}Te_{0.5}$. On average, the $\sigma_{E,50}$ value is 7 ± 1 meV/atom. Calculating the uncertainty in $\Delta\bar{H}$ using Eqs. (9) and (10) results in $\sigma_{\Delta\bar{H},50} = 1.0 \pm 0.2$ meV/atom In this particular instance, we are focused on determining the uncertainty in $\sigma_{\Delta\bar{H},50}$, not its actual value. Having an uncertainty in $\sigma_{\Delta\bar{H},50}$ of 0.2 meV/atom due to Eq. (10) is insignificant and well within the typical noise of thermodynamic calculations using DFT. We thus conclude that, for our system and property of interest, an initial ensemble size of 50 is sufficiently large such that $\sigma_{H,n} \approx \sigma_{H,\text{tot}}$. In the remainder of the results, we will adopt an n_o of 50 as a starting point for estimating $\sigma_{\bar{H},n_o}$. For a further test comparing the ΔG_{mix} for complete and random sampling, please see Fig. 2 of the Supplemental Material [48]. As detailed in Sec. II, additional configurations can then be added to the ensemble until $\sigma_{\bar{H},n'}$ is within the desired uncertainty.

3. Supercell size convergence

To disentangle the effects of random sampling from supercell size dependence, we ran our convergence tests by sampling all possible configurations from 4- to 24-atom supercells. For convergence of ΔG_{mix} with respect to the supercell size, please see Fig. 1 of the Supplemental Material [48]. The results were also compared to a large (128-atom) SQS of the same composition. Since the SQS represents the ensemble in the high-temperature limit, the SQS energy should be equivalent to the mean energy of the thermodynamic density of states, $\Delta\bar{H}$. There is always some variability between SQS cells. For the ΔH_{mix} and B, we find there is sufficiently low variability to use a single 128-atom SQS as a benchmark for convergence; see Fig. 3 of the Supplemental Material for the supporting test [48].

In Fig. 7, $\Delta\bar{H}$ begins to converge with the SQS-128 result by 12 atoms per cell, with the difference decreasing to below 3 meV/atom. However, the distribution of energies does not converge until 20–24 atoms; here complete sampling involves 200 and 1107 unique configurations, respectively. This convergence can be seen in the thermodynamic density of states and their respective standard deviations. Only minor differences are found between the 20- and 24-atom cells; the differences between the mean energy and the SQS-128 are 1.7 and 1.8 meV/atom, and the standard deviations are 4.1 and 4.1 meV/atom, respectively. Convergence with respect to supercell size and the SQS indicates that 20-atom supercells are sufficiently large to incorporate the effects of configurational disorder for this system. These results can be viewed in terms of the CLT. If one were to build an ensemble of 50 randomly sampled configurations and calculated $\Delta\bar{H}_{50}$, one would have a 68% chance of being within 0.59 meV/atom of $\Delta\bar{H}_{\text{tot}}$ (gray shaded region in Fig. 7), and a 95% chance of being within 1.18 meV/atom. Since energy is not our only property of interest, we converged the supercell size with respect to the bulk modulus. We chose the bulk modulus as a test case since it is a medium-cost property that is dependent on atomic structure. In Fig. 7(b), the 12-atom supercells are not large enough to properly represent the softening in $PbTe_{0.5}Se_{0.5}$ that comes from distortion. However, by 20 and 24 atoms, we see excellent correspondence between the ensemble average and SQS, as well as the distributions between 20 and 24 atoms. Considering the distribution for 24-atom cells, we see significant variation in B and thus obtain a $\sigma_{\bar{B},\text{tot}}$ of 5.4 GPa. From the CLT, to achieve an uncertainty of less than 1 GPa in B, we would require an ensemble with $n = 30$.

4. Local structure

By ensemble-averaging the structure of relaxed cells, we can explicitly calculate the effects of configurational disorder on short-range structural disorder. From 50 randomly relaxed cells, there are 3600 bonds and 7200 bond angles, originating from a variety of unique local atomic arrangements. The magnitude of data allows for an in-depth statistical analysis of the structure. Furthermore, unlike SQS, the ensemble structure can be calculated as a function of temperature.

At 300 K, as shown in Fig. 8, the distributions of bond lengths and bond angles have well-defined peaks. In fact, the x-axis for the bond lengths had to be stretched to three times that of 1000 and 10 000 K, just to fully include the peaks. The narrowness of the peaks can be, in part, attributed to the configurational probability distribution. At 300 K, the four lowest energy configurations make up 69% of the ensemble

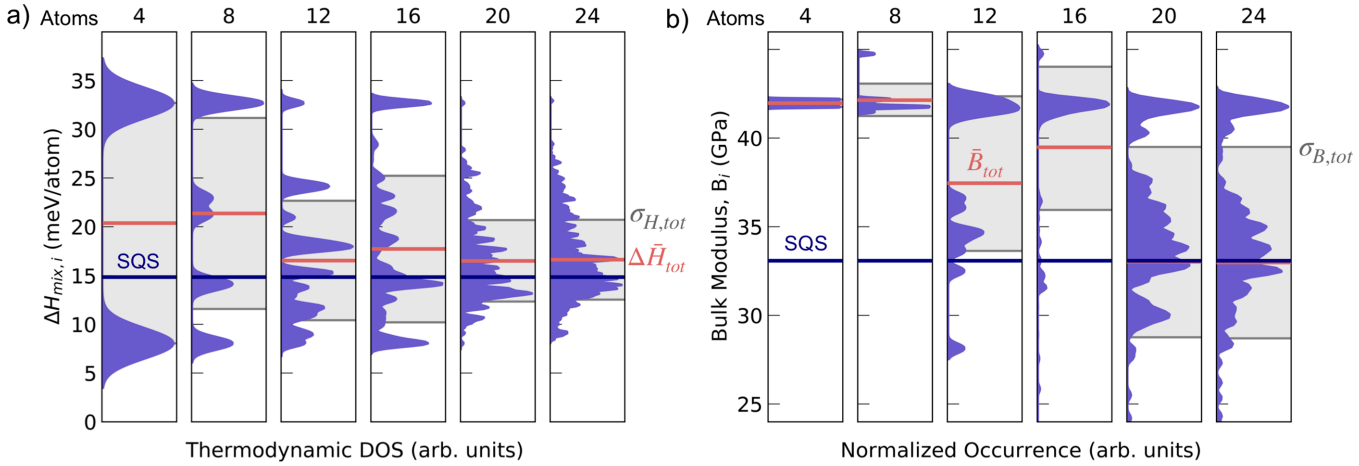

FIG. 7. (a) To assess the minimum required supercell size, we increase the supercell size for $PbSe_{0.5}Te_{0.5}$ until the distribution converges and the $\Delta\bar{H}_{tot}$ of the distribution (red) has come into agreement with the ΔH_{mix} of a 128-atom SQS supercell (blue). The convergence of the distributions can also be tracked via the $\sigma_{\Delta H,tot}$ values (gray). Here, each distribution is built from complete sampling of $PbSe_{0.5}Te_{0.5}$ for a given supercell size. (b) The importance of using larger supercells is even more visibly important for a material property like the bulk modulus. For supercell sizes of 12 and 16 atoms, the distributions are significantly different from both the properly converged 20- and 24-atom distributions and the SQS-128.

(as can be seen in Fig. 3). The degree of structural disorder is thus limited by the narrow range of structures present in the ensemble.

Within the ensemble, Pb-Se bonds are closer to the pure PbSe bond length (shown as a horizontal dashed line), but they are slightly larger due to the presence of Te. The reverse is true for Pb-Te bonds. They are shorter than that of pure PbTe. If the virtual crystal approximation were invoked [49], and $PbSe_{0.5}Te_{0.5}$ were assumed to be perfectly rocksalt, then its single, universal bond length would be 3.19 Å, derived from taking the average for that of PbSe and PbTe. There is, however, a significant gap between the two bond-length distributions, and ostensibly no amplitude at 3.19 Å. The ensemble structure is thus locally distorting from the rocksalt structure, so that the constituent bond lengths may more closely resemble the pure parent compounds. The same has been observed experimentally in $ZnSe_{1-x}Te_x$ [50] and theoretically for $PbSe_{1-x}Te_x$ [51]. The bond-angle distributions at 300 K are also relatively narrow. Angles that are made up of exclusively Se anions are obtuse to accommodate the larger Te atoms. For angles with Te as the only anion, the angles are acute, and mixed anion angles are centered around 90°, which corresponds to the ideal rocksalt structure.

As the temperature increases from 300 to 1000 K, the probability of higher-energy configurations increases as well, resulting in a smearing of the bond-length distribution. Interestingly, while the distribution of the bond length smears, the average Pb-Te and Pb-Se bond lengths remain constant (within 0.01 and 0.017 Å, respectively). Due to the smearing, there is now amplitude where there was a gap, and there is a slight peak at 3.2 Å that is shared by both distributions, corresponding to the bond length that would be derived from the virtual crystal approximation. The bond angles also significantly smear, but the average still remains at 90°, pointing to a local distortion and the structure being globally rocksalt. For bond lengths at 10 000 K, the peak at 3.2 Å grows, and since there is both Pb-Se and Pb-Te amplitude, it is roughly twice the size of the surrounding peaks. Thus, higher-energy structures that adopt a more VCA local structure (i.e., have bond lengths of 3.19 Å) are being incorporated into the ensemble. The bond-angle distributions continue to smear moving from 1000 to 10 000 K.

The same bond-length analysis was repeated for the complete set of all ∼37 000 configurations, and the resulting distributions are shown as gray dashed lines in Fig. 8. At 300 K, it can be seen that complete sampling has narrower, larger peaks than random sampling. This is to be expected. Random sampling, which samples from a uniform distribution of configurations, will have difficulty approximating a highly nonuniform distribution where the configurational probabilities vary widely, like one that is seen at 300 K. Still, the derived probabilities of the various configurations are sufficiently good to show the gap in bond lengths at 300 K. The average bond lengths at 300 K for Pb-Te and Pb-Se are 3.254 and 3.127 Å for complete sampling, and 3.253 and 3.131 Å for random sampling, showing overall good correspondence as well. Finally, at 1000 and 10 000 K, where the probability distribution for configurations is more uniform, random sampling does an excellent job of replicating the bond-length distribution obtained from complete sampling.

Analysis at high temperatures indicates that the bond length and angle distributions do not stabilize to the high-temperature limit until 10 000 K. With a melting point near 1000 K, the alloy would melt far before reaching this high-temperature limit.

B. $PbSe_{1-x}Te_x$ pseudobinary

The free-energy calculations from Fig. 5 were extended across the $PbSe_{1-x}Te_x$ system. Figure 9 plots the ΔG_{mix} for all 13 compositions as a function of temperature. The ΔG_{mix} of every alloy decreases with temperature, but this change is greater for compositions towards the center since they have larger configurational entropies. Thus, the ΔG_{mix}

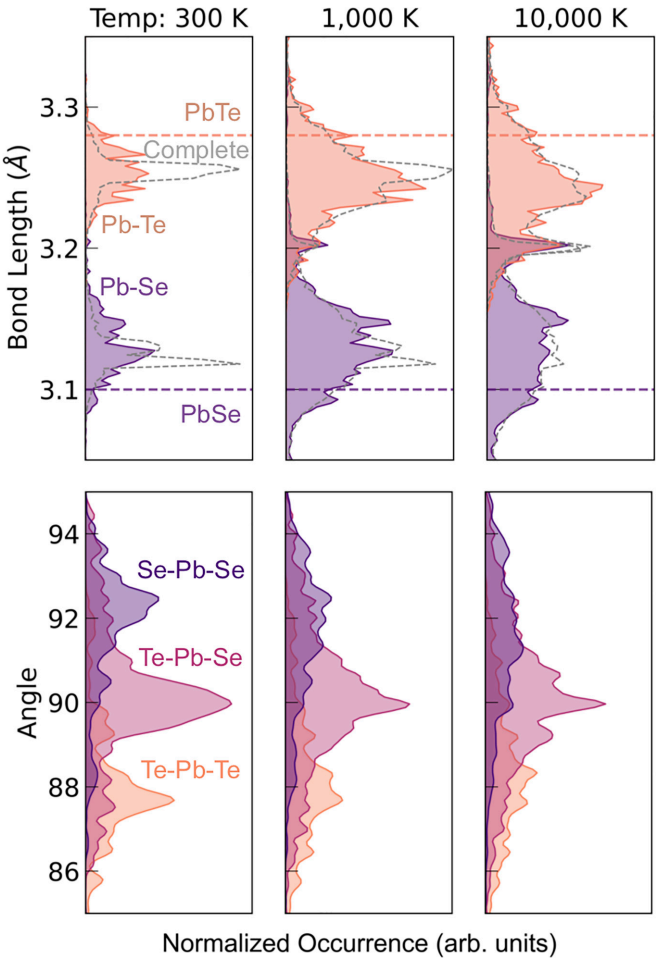

FIG. 8. At low temperature, $PbSe_{0.5}Te_{0.5}$ has distinct Pb-Te and Pb-Se bond lengths and strong clustering of bond angles. The deviation from 90° even at low temperature for these rocksalt structures highlights the internal strains present in these alloys. With increasing temperature, the distribution of bond lengths and angles broadens significantly. The x-axis of the 300 K panel has a scale that is four times larger than the 1000 and 10 000 K panels in order to accommodate the large, narrow peaks. Here, the colored distributions are for a random ensemble for 50 configurations, and the dashed lines show the complete sampling for bond lengths. Despite the low number of configurations, these structures still involve 3600 unique bonds and 7200 angles.

curve goes from being concave to convex as the temperature increases. Liu *et al.* have experimentally shown that the temperature at which full miscibility occurs is between 573 and 773 K in $PbSe_{1-x}Te_x$ and that these alloys stay fully miscible until melting [52]. These results are consistent with the typical growth temperatures (770–990 K) of $PbSe_{1-x}Te_x$ alloys [53,54].

Our results align with these experimental results, showing that $PbSe_{1-x}Te_x$ is fully miscible at 700 K, below the typical experimental growth temperatures and within the range that Liu *et al.* report. At elevated temperatures, we find that there are some compositions where the ΔG_{mix} curve is locally concave, but this deviation from convexity is 0.5–1 meV/atom, which is within the uncertainty of random sampling. More

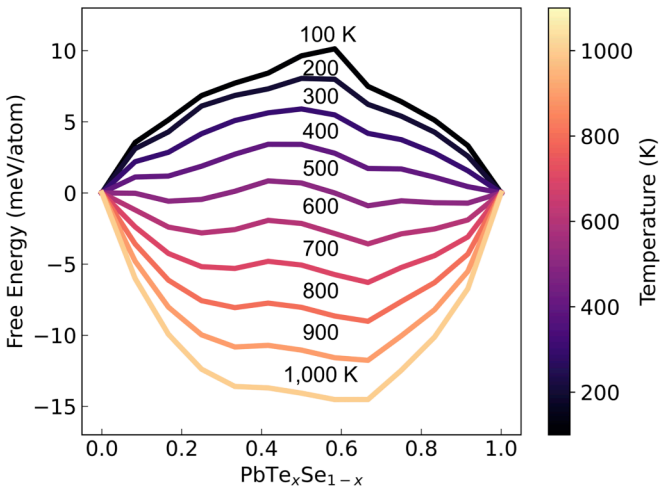

FIG. 9. The ΔG_{mix} of $PbSe_{1-x}Te_x$ gradually becomes more concave with increasing temperature, reaching full convexity at 700 K (within a tolerance of $2\sigma_{\bar{H},n}$). Here, the alloy compositions are sampled at 1/12 increments.

specifically, a composition is classified as being on the hull if its ΔG_{mix} is within $2 \times \sigma_{\Delta\bar{H},n}$ of the free-energy convex hull.

We also studied the local structure across compositions. In Fig. 10, the distribution of bond lengths is shown across the $PbSe_{1-x}Te_x$ pseudobinary. All configurations are weighed equally in these distributions, corresponding to a high-temperature ensemble average. For $PbSe_{11/12}Te_{1/12}$, the bond lengths are tightly clustered around that of PbSe, but the bonds are slightly larger due to the incorporation of the larger Te atom. The amplitude at 3.2 Å originates from Pb-Te bonds, as can be seen in the Supplemental Material [48]. The reverse

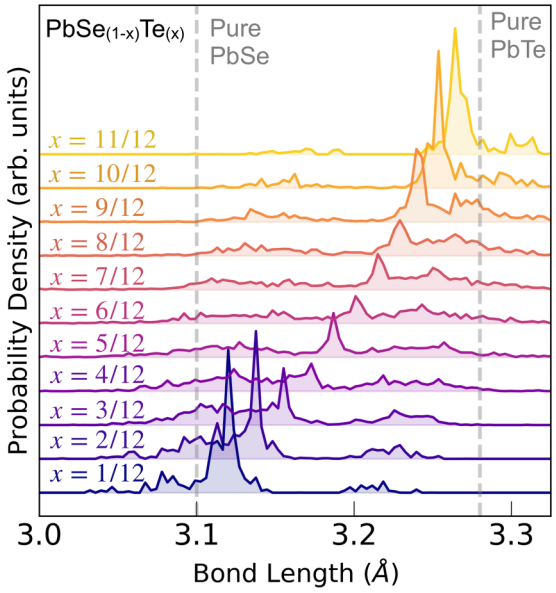

FIG. 10. Bond-length distributions in $PbSe_{1-x}Te_x$ smear as we move towards x-values of 6/12, highlighting the increased structural disorder in these alloys. The peak of each distribution corresponds well to Vegard's law. All distributions are shown in the high-temperature limit, and are generated from 50 configurations.

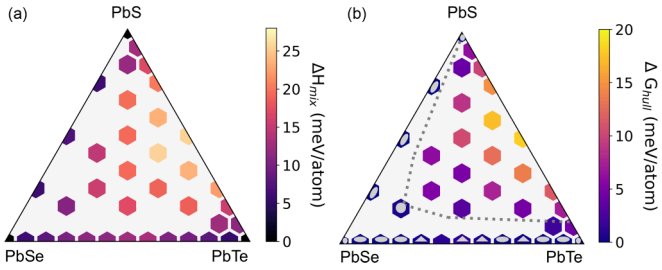

FIG. 11. (a) The calculated enthalpy of mixing (ΔH_{mix}) for the $PbS_xSe_yTe_{1-x-y}$ space is shown. ΔH_{mix} is particularly high for PbS-PbTe-rich compositions. (b) The free energy *above* the convex hull (ΔG_{hull}) finds that compositions rich in both PbS and PbTe are at energies above the hull. They are thus subject to decomposition to PbS and PbTe alloys. Gray circles denote being on the hull, and gray triangles signify that the composition is on the hull within the uncertainty from random sampling (i.e., $\Delta G_{\text{hull}} < 2\sigma_{\Delta H}$). The simulated results are corroborated by experimental findings, although there is a temperature offset. Both ΔH_{mix} and ΔG_{hull} were calculated at 600 K. The gray dashed line is an experimental result showing the region of immiscibility at 773 K [52].

trend is true for $PbSe_{1/12}Te_{11/12}$, where the slight amplitude at 3.15 Å comes from the Pb-Se bonds. For the compositions towards the middle of the pseudobinary, the bond distribution has an evidently larger spread. In part, this can be explained by simply having more diversity in the anions. If all Pb-Se and Pb-Te bonds were at a fixed length, then moving to the middle compositions would still increase the spread of the distribution. However, the spread also increases in the Pb-Se and Pb-Te bonds, as can be seen in Supplemental Fig. 4 [48]. The position of the largest peak in the distribution shifts linearly as a function of composition. The position of these peaks corresponds to Vegard's derived bond length. Vegard's law closely corresponds to the maximum peak of the distribution, but more in-depth structural techniques like this method are necessary for ascertaining the extent of structural distortions.

C. $PbS_xSe_yTe_{1-x-y}$ pseudoternary and the free-energy convex hull

Extending this methodology from pseudobinaries to pseudoternaries, we consider the $PbS_xSe_yTe_{1-x-y}$ system. The enthalpy of mixing (ΔH_{mix}) at 600 K across this chemical space is shown in Fig. 11. Within the composition space, $PbS_{0.5}Te_{0.5}$ and $PbS_{0.42}Se_{0.42}Te_{0.16}$ have the highest ΔH_{mix} values. This can be explained by PbTe and PbS having the largest volume mismatch ($\Delta V = 8$ Å^3/atom), which has been shown to be a significant factor in determining miscibility [55,56]. The ΔH_{mix} across PbTe-PbSe is lower due to the smaller size mismatch (5 Å^3/atom), and PbSe-PbS has the lowest ΔH_{mix}, corresponding to its lowest size mismatch (3 Å^3/atom). Adding significant Se to the PbS-PbTe binary reduces the ΔH_{mix}; one could rationalize this as the Se diluting the unfavorable Te-S interactions. The converse is also true: adding S to the PbSe-PbTe compositions raises its energy by increasing the concentration of S-Te interactions.

To determine which compositions of $PbS_xSe_yTe_{1-x-y}$ are stable against decomposition, ΔG_{mix} was calculated for a temperature of 600 K, and a free-energy convex hull was subsequently built from those values. The energy difference between the alloy and the free-energy convex hull at each point, ΔG_{hull}, is shown in Fig. 11(b). If a composition is on the hull, that is, the composition is stable against phase separation, then $\Delta G_{\text{hull}} = 0$. Hexagons with gray dots in them are mathematically on the hull (i.e., $\Delta G_{\text{hull}} = 0$), while hexagons with triangles are on the hull within their uncertainty (i.e., $\Delta G_{\text{hull}} < 2\sigma_{\Delta H}$). Some error is inherent in this approach as the hull is built from discrete points rather than a continuously defined ΔG_{mix} function. We find that there is a wide two-phase region along the PbS-PbTe pseudobinary. This region narrows as PbSe is added, both by decreasing the enthalpy and increasing the entropy. These predictions are consistent with prior experimental literature; Ref. [52] measured the phase-boundary edge at the dashed line 773 K and obtained the gray dashed curve in Fig. 11(b).

D. $(Pb_{1-x}Ge_x)(Te_ySe_zS_{1-y-z})$ high-entropy space

We extend the Pb-chalcogenide pseudoternary to the high-dimensional $(Pb_{1-x}Ge_x)(Te_ySe_zS_{1-y-z})$ system. Here we choose Ge for its small radius relative to Pb, which is expected to result in significant regions of immiscibility. For reference, the ionic radius of Ge is only 39% smaller than that of Pb when both have a sixfold coordination and a +2 oxidation state [57]. Ge was additionally chosen as an intriguing expansion of the composition space due to the structural diversity found in the end members (i.e., GeS, GeSe, GeTe). In their ground states, GeS and GeSe are *Pnma* and GeTe is *R*3*m* [58–60]. Finally, Ge-based chalcogen alloys have shown intriguing thermoelectric behavior [61–63].

In the study of the $(Pb_{1-x}Ge_x)(Te_ySe_zS_{1-y-z})$ system, an n_o of 50 configurations with 24-atom supercells was used for all 78 compositions. The standard deviation in the ΔH_{mix} for a given composition, $\sigma_{H,50}$, remained fairly consistent throughout the composition space. The CLT was employed to calculate the uncertainties in the ΔH_{mix} using these $\sigma_{H,50}$ values; only $Pb_{0.5}Ge_{0.5}S$ and $GeTe_{0.25}S_{0.75}$ had an uncertainty higher than 1.5 meV/atom, and all compositions were below the desired uncertainty of 2 meV/atom.

The $(Pb_{1-x}Ge_x)(Te_ySe_zS_{1-y-z})$ composition space yields a pseudohexanary alloy represented by a trigonal prism, bounded by two pseudoternaries and three square pseudoquaternaries [Fig. 12(a)]. Concerning the pseudoternary faces, the $PbS_xSe_yTe_{1-x-y}$ face has been discussed in Sec. III C. Figure 12 shows different slices through this composition space at two different temperatures.

As previously discussed, at $T = 600$ K the pseudoternary in Fig. 12(b) appears to be the most soluble judging by the number of compositions that are on the convex hull. The free energy of the opposite face, $GeS_xSe_yTe_{1-x-y}$, is shown in Fig. 12(d) at 600 K. Once again, the GeS-GeTe alloys are more energetically costly than the GeS-GeSe and GeSe-GeTe alloys. Experimental phase stability measurements indicate extremely limited solubility for GeS-GeTe [64]. There is also limited solubility for GeS-GeSe [65], despite GeS and GeSe having the same crystal structure. Experimental studies of GeSe-GeTe indicate a complete solid solution at temperatures above 930 K and narrow ranges of immiscibility at low temperature to account for changes in space group

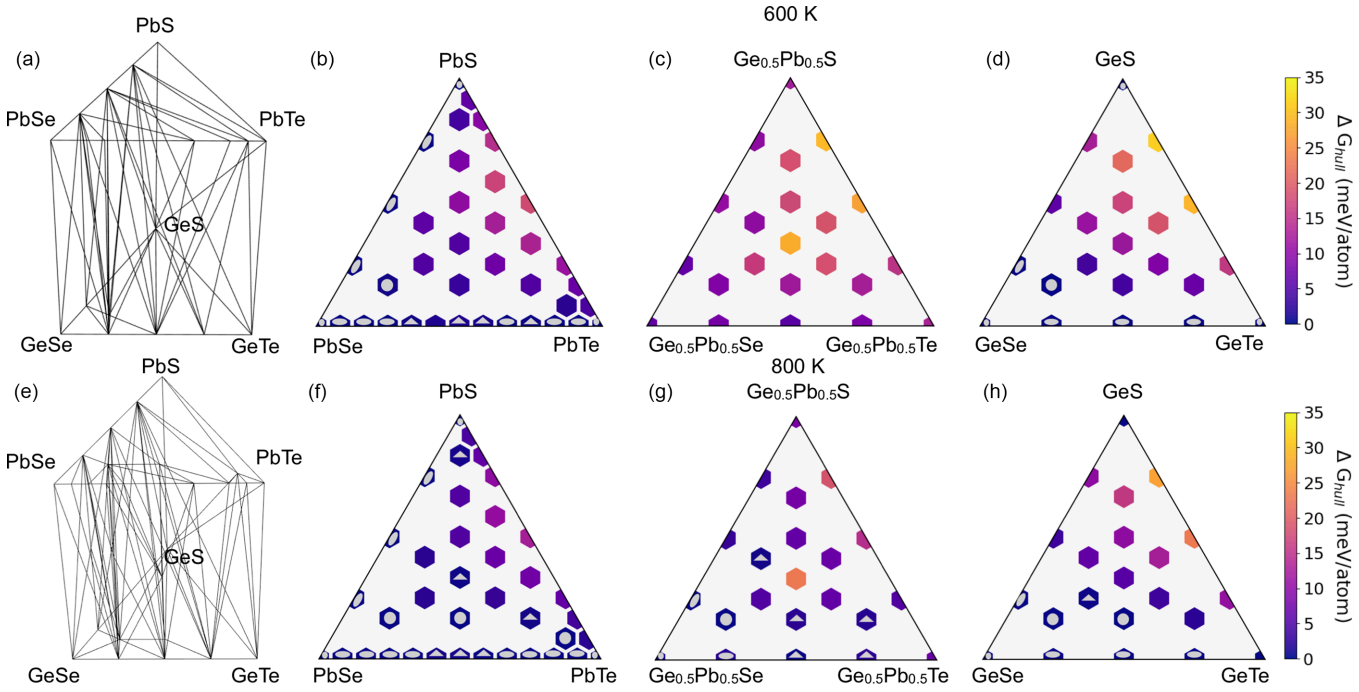

FIG. 12. (a) The $(Pb_{1-x}Ge_x)(Te_ySe_zS_{1-y-z})$ phase space is visualized as a prism with cation composition varying along the axis. Pseudoternaries (b)–(d) show three slices of this prism with discrete sampling; the color scheme denotes the free energy above the convex hull. Hexagons with a silver point inside indicate that they are on the hull; hexagons with a triangle denote compositions whose distance from the hull is less than their uncertainty ($2\sigma_{\bar{E},n}$, as determined by the CLT). Calculating the convex hull at 600 K using the coarse sampling of (b)–(d) fills the interior of the prism with four-phase tetrahedra. At this temperature, the $x = 0.5$ compositions are not on the hull, and the resulting tetrahedra of (a) span from $x = 0$ to 1 compositions. (e)–(h) The lower row shows the results at 700 K. At this temperature, far more compositions are on the hull, including in the interior of the prism (g), where many of the compositions exhibit significant entropy stabilization.

[66]. The symmetry-driven regions of immiscibility are fairly narrow, and therefore are not found using the coarse compositional sampling presented here. There is fairly little solubility reported for adding GeSe and GeS to GeTe, with phase separation occurring at the dilute concentration of $GeS_{0.05}Se_{0.05}Te_{0.9}$ [62]. The predicted tendency to decompose to GeX- and PbX-rich pseudoternaries is consistent with known $Pb_{1-x}Ge_xS$, $Pb_{1-x}Ge_xSe$, and $Pb_{1-x}Ge_xTe$ pseudobinaries [67–69]. At high temperatures, $Pb_{1-x}Ge_xTe$ is known from experiments to become miscible for a narrow temperature range before melting (843–965 K) [69].

The interior of the prism shown in Fig. 12(a) is completely filled with Alkemade tetrahedra. These four-phase regions arise from determining the convex hull of this three-dimensional composition space. It is important to note that because our calculations are limited to single points in composition space, a single-phase region can only be represented as a series of adjacent, small, multiphase regions. This discrete sampling likewise precludes a complete determination of the phase diagram at the current sampling density. However, even this limited sampling provides predictions concerning phase stability. Specifically, the $(Pb_{0.5}Ge_{0.5})(Te_ySe_zS_{1-y-z})$ compositions that are above the hull indicate a concave region in the interior of the prism. The edges of this concave region are not, however, well defined as there is likely some mixed cation solubility in the single-phase regions at the top and bottom of the prism.

Limited sampling does not provide a lower bound on the energy of the hull, but it does provide an upper bound; if a composition is found to be above the hull, no amount of increased sampling will push it onto the hull. Furthermore, if a composition is found to be on the hull, increased sampling may result in the discovery of a new low-energy composition that pushes previously found compositions off the hull. Even with the low sampling density considered herein, some preliminary insights into the free-energy surface and associated multiphase regions can be inferred from Fig. 12(a). The presence of many Alkemade tetrahedra connecting to a single point, as seen along the GeTe-GeSe edge, suggests the presence of a nearby favorable extrema (i.e., large positive Hessian) in the free-energy surface. These results are consistent with the experimental results for the pseudobinaries discussed above. To our knowledge, the interior of the prism has not been experimentally studied.

Considering the 800 K behavior of $Pb_{1-x}Ge_xTe_ySe_zS_{1-y-z}$, we predict significant stabilization of the interior ($x = 0.5$), as seen in Fig. 12(g). As expected, the lower-entropy Ge and Pb pseudoternaries show minimal increased stabilization from the 200 K increase in temperature. The resulting grid is still coarsely sampled (i.e., $x = 0, 0.5, 1$) and is likely subject to qualitative changes in the resulting phase diagram with increased density.

The middle slice of the prism [Fig. 12(g)] is entirely above the hull at 800 K. Many of these compositions are not on the free-energy convex hull due to their high ΔH_{mix} and the presence of competing alloy compositions with low ΔG_{mix}. Further, the TDOS of the nominally high-entropy calculations is sufficiently broad such that the true entropy is far lower

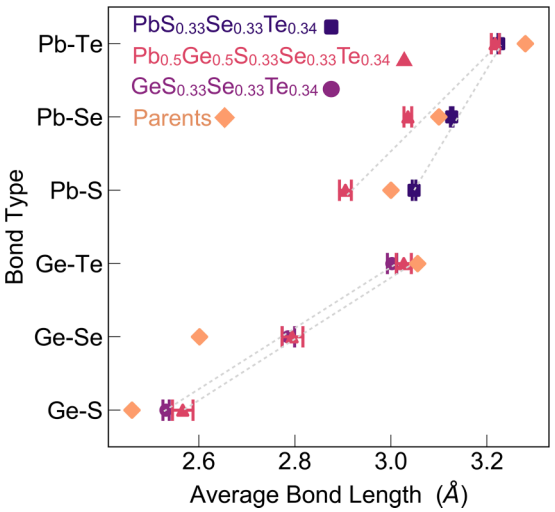

FIG. 13. Local distortion resulting in alloy bond lengths deviating from their parent bond lengths. Further complications arise when mixing parent compounds with different structures. Average bond lengths, broken up by type, are shown for various compositions. The bars denote the standard deviation in the bond lengths for a given type and composition. For reference, the parent bond lengths are included as well. We are invoking the high-temperature limit by taking simple averages. All averages are generated from 50 configurations.

than its maximum possible value, derived from the high-temperature limit. Highlighting this competition, 14 out of the 22 compositions in the middle slice have negative free energies, and thus would not decompose into their parent compounds, but due to competing alloy compositions, only half of those compositions are on the hull (within the uncertainty of the calculations). For instance, $Pb_{0.5}Ge_{0.5}S_{0.33}Se_{0.33}Te_{0.34}$ decomposes into $GeSe_{0.25}Te_{0.75}$, $GeSe_{0.5}Te_{0.5}$, $PbSe_{0.5}S_{0.5}$, and $PbSe_{0.25}S_{0.75}$. The results would have been qualitatively different if a metric like the temperature of mixing had been used since it only determines the temperature at which ΔG_{mix} is zero, thus assuming that the parent compounds are the only competing compositions. We find that the presence of competing alloy compositions is large, especially in high-entropy spaces, underlying the need for a free-energy convex hull to determine solubility.

To investigate the local structure in the center of the compositional prism, $Pb_{0.5}Ge_{0.5}S_{0.33}Se_{0.33}Te_{0.34}$, we consider bond-length trends (Fig. 13) with those of the pseudoternaries $GeS_{0.33}Se_{0.33}Te_{0.34}$ and $PbS_{0.33}Se_{0.33}Te_{0.34}$ and the parent compounds. Beginning with $PbS_{0.33}Se_{0.33}Te_{0.34}$, the Pb-*X* bond lengths are close to their parent bond lengths. However, the mixture of anions yields an average lattice constant that drives local strains. This strain is visible as the average Pb-Te bond distance shrinks and Pb-S bonds grow such that they are closer to the overall average bond length (3.1 Å). As this average bond length is close to that of PbSe, the Pb-Se bonds do not significantly distort. We also calculated the average coordination number of the composition to be 5.9, indicating the presence of structural deviations from the undistorted rocksalt with a coordination of 6.

A qualitatively similar trend exists with $GeS_{0.33}Se_{0.33}Te_{0.34}$; the Ge-Te bonds slightly shrink and the other two bond types have to grow. However, the average coordination number is 4.4, indicating a significant distortion from rocksalt. This behavior can be rationalized by examining the parent structure across the Ge chalcogenides. To start, we review structure and polymorphism in the respective parent structures. Given our algorithm for determining the first coordination shell, GeTe in the *R*3*m* space group is found to be sixfold-coordinated, and thus the plotted point is the average of its three short bonds (2.85 Å) and three long bonds (3.26 Å). We note that the trend in bond length for the Ge-*X* compounds is very consistent with the Pb-*X* compounds if only the short Ge-Te bond is considered in Fig. 13. This strong distortion can be viewed through the lens of thermodynamics; namely, the *R*3*m* structure is 17 meV/atom higher in energy than the rocksalt polymorph. GeSe and GeS (*Pnma*) show up as being threefold-coordinated, and their rocksalt polymorphs are 20 and 54 meV/atom. Given the above information about the three parents, it is reasonable that even though the Ge atoms start out octahedrally coordinated in $GeS_{0.33}Se_{0.33}Te_{0.34}$, they relax locally such that their coordination number is significantly reduced.

With this understanding of the Pb- and Ge-based pseudoternary alloys, the behavior of $Pb_{0.5}Ge_{0.5}S_{0.33}Se_{0.33}Te_{0.34}$ can be rationalized. The average coordination number is 4.3 within this alloy, and these broken bonds are evenly distributed between Ge and Pb; this is quite low given the nearly perfect octahedral coordination found in $PbS_{0.33}Se_{0.33}Te_{0.34}$. The average bond length in this compound is 3.0 Å; this leads to a shrinking of the Pb-S and Pb-Se bond lengths. In contrast, the distribution of Pb-Te bond lengths is relatively unaffected by the addition of Ge at high concentrations. Considering the Ge-*X* bonds within $Pb_{0.5}Ge_{0.5}S_{0.33}Se_{0.33}Te_{0.34}$, the addition of Pb is largely inconsequential. The average coordination number is 4.2, and the bond lengths are consistent with the $GeS_{0.33}Se_{0.33}Te_{0.34}$ pseudoternary.

IV. DISCUSSION

Having demonstrated the utility of this method in a variety of alloy spaces, here we review the strengths, identify persistent challenges, and highlight opportunities for expanding upon the current work. Broadly, we try to position this method in between two extremes for simulating alloys—using a single large supercell like SQS, and completely sampling small supercells, as has been done with other implementations of the independent cell approximation [22,24]. Working within the independent cell approximation allows for the evaluation of ensemble properties as a function of synthesis temperature. By employing random sampling, we are able to evaluate larger, more disordered supercells in a computationally efficient manner. Using these supercells allows for an in-depth evaluation of the local structure, all as a function of synthesis temperature. Lastly, random sampling provides the basis for effectively navigating the computational tradeoffs between precision and computational cost; from the central limit theorem, we derive the relationship between precision and the number of additional samples. Doing so allows for a judicious use of computational resources in exploring composition space. Furthermore, having the ability to trade off between

cost and uncertainty can be leveraged in optimal experimental design [70] and Bayesian optimization methods [71].

Nevertheless, effective use of this method requires care. It is important to be aware of polymorphism in alloys and rare configurational ground states that might not be found using limited random sampling. Furthermore, any thermodynamic methodology will suffer from the fact that there could be competing stoichiometries that push compositions off the hull.

A. Polymorphism

In the efforts herein, the polymorphic competition for the parent binaries is between three phases (rocksalt, $R3m$—a rhombohedral perturbation, and the more significant *Pnma* distortion). Within DFT relaxations, we have found continuous transitions between these structure types, and the ergodic hypothesis is thus generally satisfied. However, caution must be taken in initializing heterostructural alloys where the parents have different ground-state structures without continuous transitions between them (e.g., zinc-blende and rocksalt). Here, relaxations in DFT may only capture the local ground-state structure-type and miss the global ground state. Testing the sensitivity to starting lattice choice is, in these cases, critical. Further, *post hoc* grouping of the resulting structures based on space group and local coordination is needed to avoid incorrectly assuming ergodicity between all sampled structure types [28,29]. Another method for comparing free energies of various structure types is to start with amorphous structures rather than known crystalline prototypes, and conduct structural relaxations, as we have done in various other works [28,29]. This approach provides insight into the basins of attraction for these polymorphs and makes no assumptions about structure type.

B. Sampling limitations

In importance sampling, the target probability distribution is not directly accessible; in our case, this would be the probability of any specific configuration occurring. Instead, we randomly sample from a uniform distribution of configurations; in the event that the true probability distribution is close to random, then our method will converge with relatively fewer samples than a highly nonuniform distribution [72]. In the high-temperature limit, the true probability distribution is uniform, and at the temperatures of interest for our systems, the probability distribution is nearly uniform. As such, random sampling is an effective method to assemble an ensemble. For systems equilibrated at low temperature, or that have strong ordering tendencies, a larger number of samples will be required to accurately represent the distribution. Importantly, there are two sources of error. The first is due to incompletely sampling from a distribution of configurations, and the second is due to sampling from an erroneous distribution. The central limit theorem allows for the evaluation of the first source of error, but not the second. Thus, the central limit theorem may offer misleading guidance with respect to convergence in this situation.

In the case in which the ordered ground state is expected to be significantly more probable than other configurations, caution needs to be taken. Not finding the ground state would result in erroneous probabilities, which would affect the ensemble thermodynamics and probabilities. The challenge of highly nonuniform distributions can be addressed in a multitude of ways. First, complete sampling using small supercells can be used to partially mitigate this risk. Second, advanced Monte Carlo (MC) methods such as Metropolis-Hastings or Wang-Landau sampling can be used [73,74]. Metropolis-Hastings MC involves samples from an approximate distribution that more closely resembles the true distribution [13–15,75], and Wang-Landau approximates the TDOS directly [16,17]. MC inherently requires discarding a portion of the overall calculations, and thus requires a model Hamiltonian to make the computational cost accessible. The independent cell approximation, the central limit theorem, and model Hamiltonians are complimentary techniques; combining them would allow for the calculation of nonthermodynamic ensemble properties through the efficient sampling of highly nonuniform distributions.

V. CONCLUSION

Evaluating the stability and structure across high-dimensional alloy space is fundamental to future high-throughput searches for high-performing alloys. In this work, we implemented the independent supercell approximation, allowing for the calculation of the thermodynamics and local structure of disordered alloys. Applying this method to the (Pb,Ge)(S,Se,Te) composition space and subspaces therein, we predicted phase diagrams consistent with prior experimental literature, and we made predictions concerning the local structure. An attractive feature of this approach is the ability to estimate the uncertainty of ensemble averages using the central limit theorem, and to tune their precision by adjusting the sample size. This approach extends to a broad swath of ensemble properties, including local and long-range structure, mechanical properties, magnetic structure, thermal expansion, and both phonon and ion transport. We initially demonstrated the applicability of our methodology to ensemble properties by considering the bulk modulus of $PbSe_{0.5}Te_{0.5}$.

ACKNOWLEDGMENTS

This material is based upon work supported by the National Science Foundation under Grant No. 1729594. V.S. acknowledges support of the National Science Foundation under Grant No. 1945010. E.T. acknowledges the support of the National Science Foundation under Grants No. 1940199 and No. 2118201. R.G. also recognizes the support of the National Science Foundation under Grants No. 1940224 and No. 1845434. The use of the Colorado School of Mines's computing resources is gratefully acknowledged.

[1] R. R. Schnepf, J. J. Cordell, M. B. Tellekamp, C. L. Melamed, A. L. Greenaway, A. Mis, G. L. Brennecka, S. Christensen, G. J. Tucker, E. S. Toberer, S. Lany, and A. C. Tamboli, Utilizing site disorder in the development of new

energy-relevant semiconductors, ACS Energy Lett. **5**, 2027 (2020).
[2] R. R. King, D. C. Law, K. M. Edmondson, C. M. Fetzer, G. S. Kinsey, H. Yoon, R. Sherif, and N. H. Karam, 40% efficient metamorphic GaInP/GaInAs/Ge multijunction solar cells, Appl. Phys. Lett. **90**, 183516 (2007).
[3] J. F. Geisz, R. M. France, K. L. Schulte, M. A. Steiner, A. G. Norman, H. L. Guthrey, M. R. Young, T. Song, and T. Moriarty, Six-junction III–V solar cells with 47.1% conversion efficiency under 143 Suns concentration, Nat. Energy **5**, 326 (2020).
[4] I. T. Witting, T. C. Chasapis, F. Ricci, M. Peters, N. A. Heinz, G. Hautier, and G. J. Snyder, The thermoelectric properties of bismuth telluride, Adv. Electron. Mater. **5**, 1800904 (2019).
[5] C. Oses, C. Toher, and S. Curtarolo, High-entropy ceramics, Nat. Rev. Mater. **5**, 295 (2020).
[6] A. Zunger, S. H. Wei, L. G. Ferreira, and J. E. Bernard, Special Quasirandom Structures, Phys. Rev. Lett. **65**, 353 (1990).
[7] L. G. Ferreira, S. H. Wei, and A. Zunger, First-principles calculation of alloy phase diagrams: The renormalized-interaction approach, Phys. Rev. B **40**, 3197 (1989).
[8] C. Jiang and B. P. Uberuaga, Efficient *Ab initio* Modeling of Random Multicomponent Alloys, Phys. Rev. Lett. **116**, 105501 (2016).
[9] G. S. Pomrehn, E. S. Toberer, G. J. Snyder, and A. van de Walle, Entropic stabilization and retrograde solubility in Zn_4Sb_3, Phys. Rev. B **83**, 094106 (2011).
[10] K. Biswas and S. Lany, Energetics of quaternary III-V alloys described by incorporation and clustering of impurities, Phys. Rev. B **80**, 115206 (2009).
[11] D. A. Keen and A. L. Goodwin, The crystallography of correlated disorder, Nature (London) **521**, 303 (2015).
[12] A. Simonov and A. L. Goodwin, Designing disorder into crystalline materials, Nat. Rev. Chem. **4**, 657 (2020).
[13] J. J. Cordell, J. Pan, A. C. Tamboli, G. J. Tucker, and S. Lany, Probing configurational disorder in $ZnGeN_2$ using cluster-based Monte Carlo, Phys. Rev. Mater. **5**, 024604 (2021).
[14] C. Wolverton, V. Ozoliņš, and A. Zunger, First-principles theory of short-range order in size-mismatched metal alloys: Cu-Au, Cu-Ag, and Ni-Au, Phys. Rev. B **57**, 4332 (1998).
[15] A. Walle and G. Ceder, Automating first-principles phase diagram calculations, J. Phase Equilib. **23**, 348 (2002).
[16] B. Yang, M. Asta, O. Mryasov, T. Klemmer, and R. Chantrell, The nature of A1–$L1_0$ ordering transitions in alloy nanoparticles: A Monte Carlo study, Acta Mater. **54**, 4201 (2006).
[17] Z. Pei, R. Li, M. C. Gao, and G. M. Stocks, Statistics of the nicocr medium-entropy alloy: Novel aspects of an old puzzle, npj Comput. Mater. **6**, 122 (2020).
[18] A. Zunger and J. E. Jaffe, Structural Origin of Optical Bowing in Semiconductor Alloys, Phys. Rev. Lett. **51**, 662 (1983).
[19] B. R. Ortiz, H. Peng, A. Lopez, P. A. Parilla, S. Lany, and E. S. Toberer, Effect of extended strain fields on point defect phonon scattering in thermoelectric materials, Phys. Chem. Chem. Phys. **17**, 19410 (2015).
[20] R. Gurunathan, R. Hanus, and G. J. Snyder, Alloy scattering of phonons, Mater. Horiz. **7**, 1452 (2020).
[21] R. Gurunathan, S. Sarker, C. K. Borg, J. Saal, L. Ward, A. Mehta, and G. J. Snyder, Mapping thermoelectric transport in a multicomponent alloy space, Adv. Electron. Mater. **8**, 2200327 (2022).
[22] K. Yang, C. Oses, and S. Curtarolo, Modeling off-stoichiometry materials with a high-throughput ab-initio approach, Chem. Mater. **28**, 6484 (2016).
[23] Y. Lederer, C. Toher, K. S. Vecchio, and S. Curtarolo, The search for high entropy alloys: A high-throughput ab-initio approach, Acta Mater. **159**, 364 (2018).
[24] P. Sarker, T. Harrington, C. Toher, C. Oses, M. Samiee, J.-P. Maria, D. W. Brenner, K. S. Vecchio, and S. Curtarolo, High-entropy high-hardness metal carbides discovered by entropy descriptors, Nat. Commun. **9**, 4980 (2018).
[25] R. Woods-Robinson, V. Stevanović, S. Lany, K. N. Heinselman, M. K. Horton, K. A. Persson, and A. Zakutayev, Role of disorder in the synthesis of metastable zinc zirconium nitrides, Phys. Rev. Mater. **6**, 043804 (2022).
[26] P. Gorai, E. S. Toberer, and V. Stevanović, Thermoelectricity in transition metal compounds: the role of spin disorder, Phys. Chem. Chem. Phys. **18**, 31777 (2016).
[27] J. Du, O. Malyi, S.-L. Shang, Y. Wang, X.-G. Zhao, F. Liu, A. Zunger, and Z.-K. Liu, Density functional thermodynamic description of spin, phonon and displacement degrees of freedom in antiferromagnetic-to-paramagnetic phase transition in $YNiO_3$, Mater. Today Phys. **27**, 100805 (2022).
[28] V. Stevanović, Sampling Polymorphs of Ionic Solids using Random Superlattices, Phys. Rev. Lett. **116**, 075503 (2016).
[29] E. B. Jones and V. Stevanović, Polymorphism in elemental silicon: Probabilistic interpretation of the realizability of metastable structures, Phys. Rev. B **96**, 184101 (2017).
[30] F. Therrien, E. B. Jones, and V. Stevanović, Metastable materials discovery in the age of large-scale computation, Appl. Phys. Rev. **8**, 031310 (2021).
[31] E. B. Jones and V. Stevanović, The glassy solid as a statistical ensemble of crystalline microstates, npj Comput. Mater. **6**, 56 (2020).
[32] E. Perim, D. Lee, Y. Liu, C. Toher, P. Gong, Y. Li, W. N. Simmons, O. Levy, J. J. Vlassak, J. Schroers, and S. Curtarolo, Spectral descriptors for bulk metallic glasses based on the thermodynamics of competing crystalline phases, Nat. Commun. **7**, 12315 (2016).
[33] M. Esters, A. Smolyanyuk, C. Oses, D. Hicks, S. Divilov, H. Eckert, X. Campilongo, C. Toher, and S. Curtarolo, QH-POCC: taming tiling entropy in thermal expansion calculations of disordered materials, Acta Mater. **245**, 118594 (2023).
[34] M. Esters, C. Oses, D. Hicks, M. J. Mehl, M. Jahnátek, M. D. Hossain, J.-P. Maria, D. W. Brenner, C. Toher, and S. Curtarolo, Settling the matter of the role of vibrations in the stability of high-entropy carbides, Nat. Commun. **12**, 5747 (2021).
[35] S. G. Kwak and J. H. Kim, Central limit theorem: The cornerstone of modern statistics, Kor. J. Anesthesiology **70**, 144 (2017).
[36] H. Fischer, *A History of the Central Limit Theorem: From Classical to Modern Probability Theory* (Springer, New York, NY, 2011).
[37] G. L. W. Hart and R. W. Forcade, Algorithm for generating derivative structures, Phys. Rev. B **77**, 224115 (2008).
[38] G. Kresse and J. Furthmüller, Comput. Mater. Sci. **6**, 15 (1996).
[39] M. d'Avezac, P. Graf, T. Paudal, H. Peng, L. Zhang, S. Stephen, and V. Stevanovic, Pylada computational framework (2014), https://github.com/pylada/pylada-light.
[40] M. R. Islam, Sample size and its role in central limit theorem (CLT), Computat. Appl. Math. J. **4**, 1 (2018).

[41] H. Mendez, *Understanding the Central Limit Theorem* (University of California Press, Santa Barbara, CA, 1991), p. 281.

[42] J. P. Perdew, K. Burke, and M. Ernzerhof, Generalized Gradient Approximation Made Simple, Phys. Rev. Lett. **77**, 3865 (1996).

[43] P. E. Blöchl, Projector augmented-wave method, Phys. Rev. B **50**, 17953 (1994).

[44] A. van de Walle, P. Tiwary, M. De Jong, D. L. Olmsted, M. Asta, A. Dick, D. Shin, Y. Wang, L.-Q. Chen, and Z.-K. Liu, Efficient stochastic generation of special quasirandom structures, Calphad **42**, 13 (2013).

[45] F. Birch, Finite elastic strain of cubic crystals, Phys. Rev. **71**, 809 (1947).

[46] F. D. Murnaghan, The compressibility of media under extreme pressures, Proc. Natl. Acad. Sci. (USA) **30**, 244 (1944).

[47] A. Reuss, Berechnung der fließgrenze von mischkristallen auf grund der plastizitätsbedingung für einkristalle, Z. Angew. Math. Mech. **9**, 49 (1929).

[48] See Supplemental Material at http://link.aps.org/supplemental/10.1103/PhysRevMaterials.7.063801 for various convergence tests, more information about the $PbSe_{1-x}Te_x$ bond-length distribution, and for instructions on implementing the central limit theorem at finite temperatures.

[49] L. Bellaiche and D. Vanderbilt, Virtual crystal approximation revisited: Application to dielectric and piezoelectric properties of perovskites, Phys. Rev. B **61**, 7877 (2000).

[50] P. F. Peterson, T. Proffen, I. K. Jeong, S. J. L. Billinge, K. S. Choi, M. G. Kanatzidis, and P. G. Radaelli, Local atomic strain in $ZnSe_{1-x}Te_x$ from high real-space resolution neutron pair distribution function measurements, Phys. Rev. B **63**, 165211 (2001).

[51] J. W. Doak and C. Wolverton, Coherent and incoherent phase stabilities of thermoelectric rocksalt IV-VI semiconductor alloys, Phys. Rev. B **86**, 144202 (2012).

[52] H. Liu and L. Chang, Phase relations in the system PbS-PbSe-PbTe, Mineral. Mag. **58**, 567 (1994).

[53] B. R. Ortiz, J. M. Adamczyk, K. Gordiz, T. Braden, and E. S. Toberer, Towards the high-throughput synthesis of bulk materials: Thermoelectric PbTe–PbSe–SnTe–SnSe alloys, Mol. Syst. Des. Eng. **4**, 407 (2019).

[54] Q. Zhang, F. Cao, W. Liu, K. Lukas, B. Yu, S. Chen, C. Opeil, D. Broido, G. Chen, and Z. Ren, Heavy doping and band engineering by potassium to improve the thermoelectric figure of merit in p-type PbTe, PbSe, and $PbTe_{1-y}Se_y$, J. Am. Chem. Soc. **134**, 10031 (2012).

[55] W. Hume-Rothery and H. M. Powell, On the theory of superlattice structures in alloys, Z. Kristallogr.-Cryst. Mater. **91**, 23 (1935).

[56] D. Usanmaz, P. Nath, J. J. Plata, G. L. W. Hart, I. Takeuchi, M. B. Nardelli, M. Fornari, and S. Curtarolo, First principles thermodynamical modeling of the binodal and spinodal curves in lead chalcogenides, Phys. Chem. Chem. Phys. **18**, 5005 (2016).

[57] R. D. Shannon, Revised effective ionic radii and systematic studies of interatomic distances in halides and chalcogenides, Acta Crystallogr. A **32**, 751 (1976).

[58] G. Bissert and K.-F. Hesse, Verfeinerung der struktur von germanium (II)-sulfid, GeS, Acta Crystallogr. B **34**, 1322 (1978).

[59] P. A. Murgatroyd, M. J. Smiles, C. N. Savory, T. P. Shalvey, J. E. N. Swallow, N. Fleck, C. M. Robertson, F. Jackel, J. Alaria, J. D. Major, D. O. Scanlon, and T. D. Veal, Gese: Optical spectroscopy and theoretical study of a van der Waals solar absorber, Chem. Mater. **32**, 3245 (2020).

[60] M. Samanta, T. Ghosh, R. Arora, U. V. Waghmare, and K. Biswas, Realization of both n-and p-type GeTe thermoelectrics: Electronic structure modulation by $AgBiSe_2$ alloying, J. Am. Chem. Soc. **141**, 19505 (2019).

[61] S. Perumal, S. Roychowdhury, and K. Biswas, High performance thermoelectric materials and devices based on GeTe, J. Mater. Chem. C **4**, 7520 (2016).

[62] M. Samanta and K. Biswas, Low thermal conductivity and high thermoelectric performance in $(GeTe)_{1-2x}(GeSe)_x(GeS)_x$: Competition between solid solution and phase separation, J. Am. Chem. Soc. **139**, 9382 (2017).

[63] J. M. Adamczyk, F. A. Bipasha, G. A. Rome, K. Ciesielski, E. Ertekin, and E. S. Toberer, Symmetry breaking in $Ge_{1-x}Mn_xTe$ and the impact on thermoelectric transport, J. Mater. Chem. A **10**, 16468 (2022).

[64] S. M. Lacordaire, J. Rivet, P. Khodadad, J. Flahaut, *GeS-GeTe Phase Diagram, ASM Alloy Phase Diagrams Database*, edited by P. Villars, H. Okamoto, and K. Cenzual (ASM International, Materials Park, OH, 2016).

[65] N. N. Koren, V. V. Kindyak, and E. Matyas, Phase diagram of the system GeS-GeSe, Phys. Status Solidi A **80**, K105 (1983).

[66] H. Wiedemeier and P. A. Siemers, The temperature-composition phase diagram of the GeSe-GeTe system, in *Modern High Temperature Science: A Collection of Research Papers from Scientists, Post-Doctoral Associates, and Colleagues of Professor Leo Brewer in celebration of his 65th birthday* (Humana Press, Totowa, NJ, 1984), pp. 395–408.

[67] R. L. Magunov, Y. V. Belyuga, and R. L. Magunov, PbS-GeS Phase Diagram, *ASM Alloy Phase Diagrams Database*, edited by P. Villars, H. Okamoto, and K. Cenzual (ASM International, Materials Park, OH, 2016).

[68] L. E. Shelimova, N. Abrikosov, V. V. Zhdanova, and V. V. Sizov, PbSe-GeSe Phase Diagram, *ASM Alloy Phase Diagrams Database*, edited by P. Villars, H. Okamoto, and K. Cenzual (ASM International, Materials Park, OH, 2016).

[69] L. Yashina and V. Leute, The phase diagrams of the quasibinary systems (Pb,Ge)Te and (Ge,Sn)Te, J. Alloys Compd. **313**, 85 (2000).

[70] B. Settles, Active learning literature survey, Computer Sciences Technical Report, No. 1648, University of Wisconsin–Madison, 2009.

[71] R. Garnett, *Bayesian Optimization* (Cambridge University Press, 2023).

[72] S. T. Tokdar and R. E. Kass, Importance sampling: A review, WIREs Comp. Stat. **2**, 54 (2010).

[73] K. Binder, D. Heermann, L. Roelofs, A. J. Mallinckrodt, and S. McKay, Monte Carlo simulation in statistical physics, Comput. Phys. **7**, 156 (1993).

[74] F. Wang and D. P. Landau, Efficient, Multiple-Range Random Walk Algorithm to Calculate the Density of States, Phys. Rev. Lett. **86**, 2050 (2001).

[75] S. K. Wallace, J. M. Frost, and A. Walsh, Atomistic insights into the order–disorder transition in Cu_2ZnSnS_4 solar cells from Monte Carlo simulations, J. Mater. Chem. A **7**, 312 (2019).